Nuclear Science and Techniques (2023) 34:125
https://doi.org/10.1007/s41365-023-01274-4

Source-less density measurement using an adaptive neutron-induced gamma correction method

Qiong Zhang[1] · Yi Ge[1] · Yu-Lian Li[1]

Received: 22 February 2023 / Revised: 20 April 2023 / Accepted: 16 May 2023 / Published online: 28 August 2023

Abstract
The use of radioactive isotopes, such as Cs-137, to measure formation density is a common practice; however, it poses high risks such as environmental contamination from lost sources. To address these challenges, the use of pulsed neutron sources for density measurements, also known as "source-less density", has emerged as a promising alternative. By collecting gamma counts at different time gates according to the duty cycle of the pulsed sequence, the inelastic gamma component can be isolated to obtain more accurate density measurements. However, the collection of gamma rays during the neutron burst-on period often contains a proportion of capture gamma rays, which can reduce the accuracy of density measurements. This proportion can vary depending on the formation environment and neutron duty cycle. To address these challenges, an adaptive capture gamma correction method was developed for density measurements. This method distinguishes between "burst-on" and "burst-off" periods based on the gamma time spectra, and derives the capture ratio in the burst-on period by iteratively fitting the capture gamma time spectra, resulting in a more accurate net inelastic gamma. This method identifies the end of the pulse by automatically calculating the differential, and fits the capture gamma time spectra using Gaussian process regression, which considers the differences in formation attenuation caused by different environments. The method was verified through simulations with errors of below 0.025 g/cm^3, demonstrating its adaptability and feasibility for use in formation density measurements. Overall, the proposed method has the potential to minimize the risks associated with radioactive isotopes and improve the accuracy of density measurements in various duty cycles and formation environments.

Keywords Neutron-induced gamma · Adaptive correction · Source-less density

1 Introduction

The density of formation is a critical property that plays an indispensable role in reservoir evaluation [1, 2]. Traditionally, the chemical source Cs-137 has been used in nuclear well logging to measure the formation density [3]. However, the use of this source presents significant risks, including radiation hazards to field workers and potential environmental pollution if the source is lost [1]. To address these issues, the use of safer, controllable sources such as X-ray tubes and pulsed neutron generators has increased in the field [4–9]. Pulsed neutron generators are particularly effective in complicated wells because they emit high-energy neutrons that interact with the formation to generate secondary gamma rays with higher energies than those generated by Cs-137 sources, as shown in Fig. 1. In addition, high-energy neutrons emitted by pulsed neutron generators have good monochromaticity and extensive research exists on them. Pulsed neutron logging has been extensively researched, with established methods including measuring sigma, porosity, and elemental weight fractions based on thermal neutron time spectra or inelastic and capture gamma spectra [10–15]. However, density measurements using pulsed neutrons, also known as "source-less density measurement," presents a greater challenge, compared to chemical source density measurements [16]. These measurements are influenced by both neutron and gamma fields, resulting in a lower

---

This work was supported by the National Natural Science Foundation of China (No. 52171253) and the Natural Science Foundation of Sichuan (No. 2022NSFSC0949).

✉ Qiong Zhang
zhanqio@uestc.edu.cn

[1] University of Electronic Science and Technology of China, Chengdu 610000, China

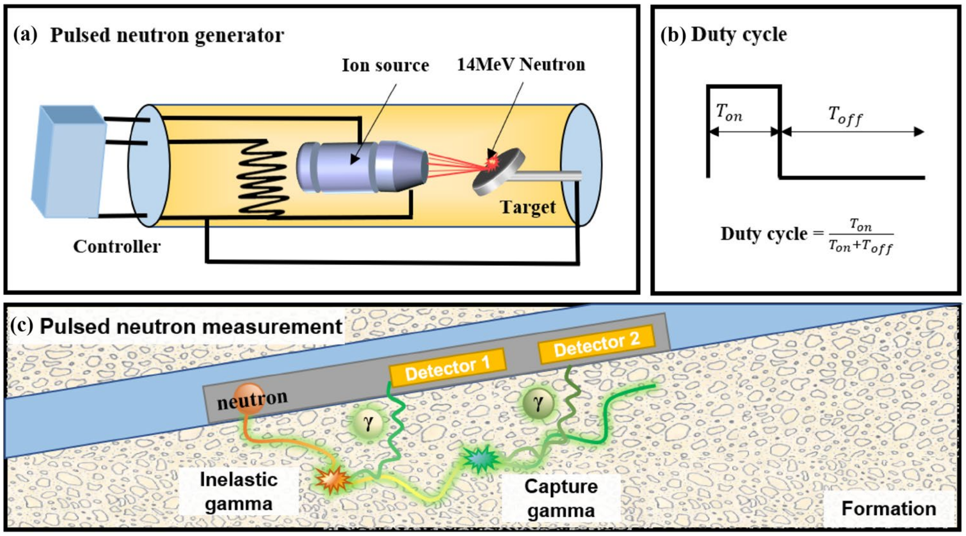

Fig. 1 (Color online) Pulsed neutron measurement process. **a** Pulsed neutron generator diagram. **b** A single duty cycle in which the periodic generation of neutrons is controlled by electric pulses. **c** Neutron-induced gamma produced in the formation during logging

density sensitivity [17]. Currently, Schlumberger is the only company offering a commercially available source-less density tool. The initial field trials have been extremely well received [18–20].

In recent years, progress has been made in the field of source-less density measurements. Reichel et al. used a thermal neutron detector count to eliminate the influence of fast neutrons on the inelastic gamma count and calculated formation density [18]. Based on the fast-neutron gamma coupled field theory, Zhang et al. have quantified the influence of the formation parameters on the inelastic gamma-field distribution and proposed a density algorithm using the fast neutron count and near-to-far detector gamma count ratio [21]. Wang et al. use the high- and low-energy windows of net inelastic gamma spectra to improve the accuracy of the formation density by reducing the influence of pair production [22]. Zhang et al. develop a new source-less density measurement method using a boron sleeve gamma detector for high-brine oil and gas formations [23]. Dong et al. have treated the source-less density measurement as a regression problem and determine the net inelastic gamma ratio, fast neutron ratio, and borehole diameter from variables to calculate the density [24]. In addition to using inelastic gamma to measure the density, Zhang et al. compare and summarize three HI correction methods [25]. In these studies, the net inelastic gamma count ratio is directly used to calculate the density. In actual measurements, neutron-induced gamma rays are collected using time gates after neutron emission [18]. This means that during the neutron “burst-on” period, the collected gamma will inevitably contain some capture gamma rays; therefore, they must be corrected to obtain the net inelastic gamma, otherwise the accuracy of the density measurement will be affected.

The gamma collected during the “burst-off” period (within a time gate of a few microseconds after neutron emission stops) can be approximately regarded as the capture gamma spectra. Therefore, if the capture gamma rays during the burst-on period can be calculated by matching the capture spectra during the burst-off period, net inelastic gamma counts can be obtained. Typically, the capture gamma is subtracted from the total gamma using a fixed proportional coefficient to obtain the net inelastic gamma count [26]. The methods for calculating fixed coefficients can be classified into two types: one is based on energy spectra only, and the other uses both energy and time spectra. Yuan et al. divided the gamma energy spectra into six energy ranges to obtain deduction coefficients and improved the accuracy of obtaining the concentration of elements by decomposing the inelastic gamma energy spectra [27]. Odom used a single exponential decay function to fit the time spectra for the capture gamma proportion [28], and Schmid and Li et al. use a double-exponential decay function to fit the time spectra to compensate for the borehole environment [29, 30].

Despite the availability of various methods for measuring the formation density, certain challenges remain unresolved. In real-world scenarios, the stability of the duty cycle varies according to the designated pulsed neutron tube. Furthermore, during downhole measurements, the environment changes according to the tool logs per vertical depth. Both challenges have significant effects on the capture gamma spectra. An example is shown in Fig. 2, where the capture gamma counts increase by 30.7% during the burst-on period when the duty cycle increases from 20 to 40%. The capture gamma counts decrease by 48% when the porosity increases from 0.9 p.u. to 20 p.u.

Under such circumstances, previously reviewed methods can no longer prove efficient. This is because these methods employ a fixed decay function, such as the double-exponential function, which cannot properly handle multiple changeable parameters, such as the duty cycle, and environmental

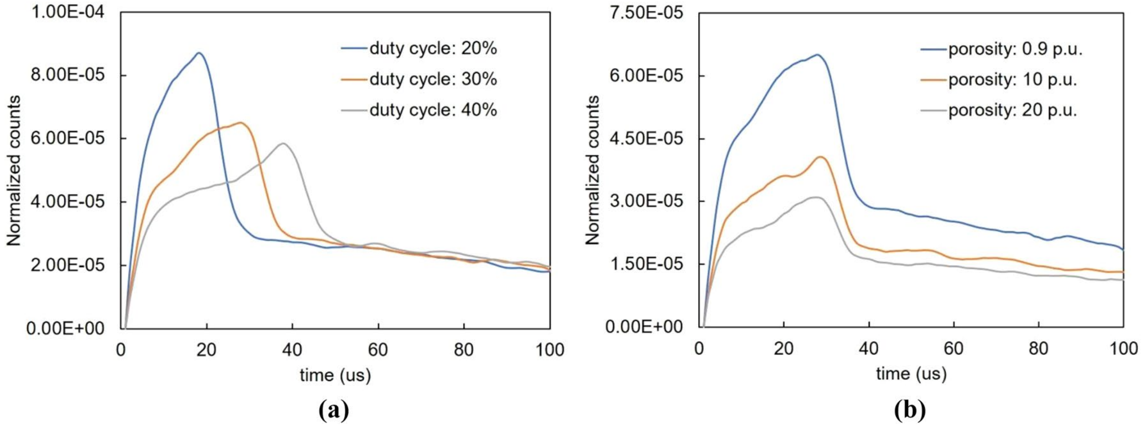

Fig. 2 (Color online) Capture time spectra changes pertaining to the duty cycle (**a**) and formation porosity (**b**)

factors, such as lithology, porosity, and borehole. This requires the manual adjustment of function-related parameters with respect to different duty cycles and environmental parameters, which hinders their ability to accurately capture gamma spectra.

To address these challenges, Gaussian process regression (GPR) was employed to develop an effective method for accurate neutron-induced gamma measurements [31]. This is caused by the following: (1) the kernel function in GPR provides an extremely strong fitting capability, which allows the time spectra obtained with different parameters to be adaptively matched, thus overcoming the limitations of fixed functions. (2) GPR is suitable for small-sample fitting, making it ideal for fitting data points (small numbers) collected within a single-pulse period. Typically, the actual time spectra are collected at time intervals of 1 and 100 µs as a pulse period, and data are acquired across multiple pulse periods to ensure the repeatability of the obtained time spectra. Consequently, the true sample data (average of the time spectra over multiple pulse periods) available for fitting are typically only 100 sample data points; thus, GPR can effectively handle such data. Using GPR to calculate the capture time spectra has the added benefit of providing probabilistic models, thus enabling statistical error analysis for effective data quality control.

Figure 3 provides an overview of the proposed method, which uses GPR to compensate for the impact of capture gamma rays during burst-on periods and obtain accurate formation densities. The proposed method comprises three main steps. First, the time spectra are matched based on the pulse characteristics to distinguish between burst-on and burst-off periods and adapt to different duty cycles. Second, GPR fits the gamma time spectra under burst-off periods to extract the capture gamma time spectra more accurately. Finally, net inelastic gamma is obtained using the capture gamma time spectra. The rest of the paper is organized as follows: Sect. 2 provides a step-by-step discussion of the proposed method, which employs a GPR algorithm framework. Section 3 presents the verification results of the proposed method based on Monte Carlo modelling under different duty cycles and formation environments. Finally, the conclusions are presented in Sect. 4.

2 Methodology

2.1 Neutron-induced gamma time spectra feature analysis

A. Overview of neutron-induced gamma: capture versus inelastic

To separate the capture and inelastic gamma rays collected during the burst-off period, it is necessary to analyze both types of gamma rays generated by the reaction. This involves the interaction of 14 MeV fast neutrons emitted by the D–T pulsed neutron generator with the formation, resulting in the production of secondary gamma rays through inelastic scattering and radiative capture. Based on one-group diffusion theory, the flux distribution of fast neutrons $\phi_{\mathrm{N}}(r)$ at r can be expressed as Eq. (1):

$$\phi_{\mathrm{N}}(r) = \frac{S_0}{4\pi r^2} e^{-r/\lambda_{\mathrm{s}}}, \tag{1}$$

where S_0 denotes the neutron strength, λ_{s} denotes the neutron slowing-down length, and r denotes the distance from the pulsed neutron source.

The probability of inelastic collisions between fast neutrons and nuclides is determined by the inelastic scattering cross section, which varies for different nuclides. Therefore, the source of secondary inelastic gamma rays in the

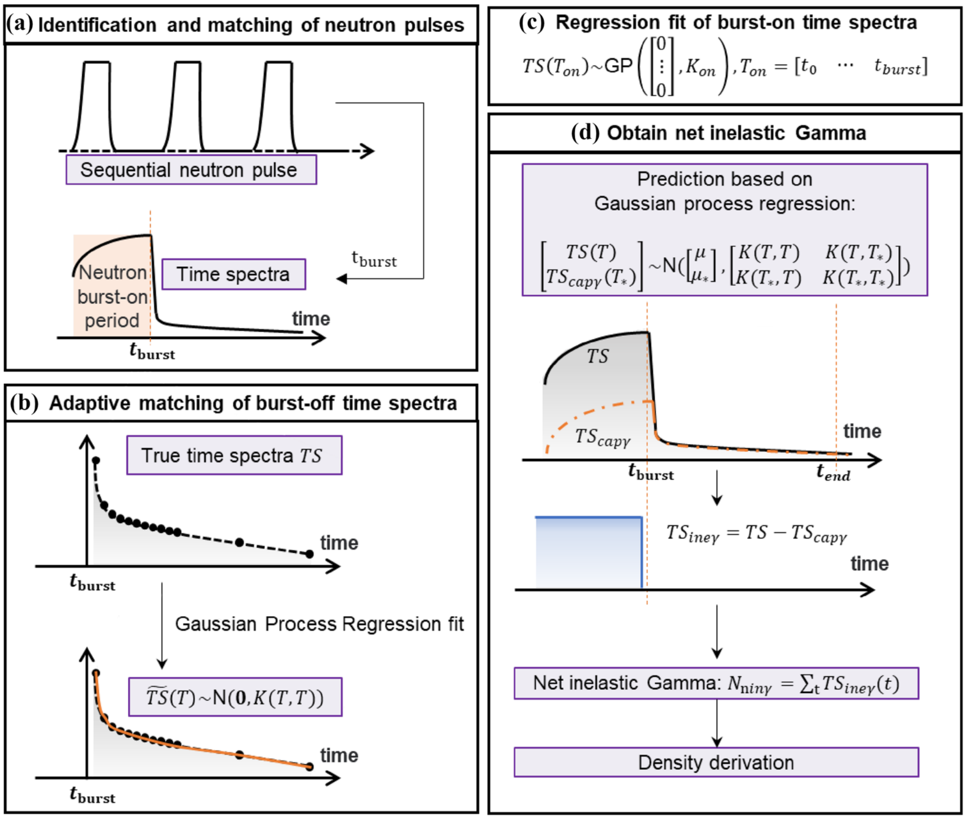

Fig. 3 (Color online) Overview of the neutron-induced capture gamma correction method

formation can be described as a set of inelastic gamma sources of M nuclides, as shown in Eq. (2).

$$S(r) = \sum_{i}^{M} S_i(r) = \sum_{i}^{M} N_i \int \phi_N(r) \sum_{\text{ine}\_i}, \tag{2}$$

where N_i is the number of gammas produced by the ith nuclide under fast neutron collisions, and $\sum_{\text{ine}\_i}$ is the inelastic scattering cross section of the ith nuclide.

Using the Lagrange median value theorem, the inelastic gammas $\phi_{\text{in}\gamma}(R)$ detected at R can be expressed as

$$\phi_{\text{in}\gamma}(R) = \frac{S_0 \sum_i^M N_i \int \sum_{\text{ine}\_i}}{4\pi R} e^{-R[1/\lambda_s - \alpha(1/\lambda_s - \mu\rho)]}, \tag{3}$$

where $\alpha \in (0, 1)$ is the proportional coefficient from Lagrange's median value theorem, ρ represents the bulk density of formation, and μ is the mass absorption coefficient.

According to the thermal neutron diffusion theory, the thermal neutron flux mainly originates from fast neutron slowing-down and thermal neutron diffusion. Therefore, the thermal neutron flux distribution is given by Eq. (4):

$$\phi_t(r) = \frac{S_0 L_t^2}{4\pi r\left(\lambda_s^2 - L_t^2\right)} \left(\frac{e^{-r/\lambda_s}}{r} - \frac{e^{-r/L_t}}{r}\right), \tag{4}$$

where $\phi_t(r)$ refers to the thermal neutron flux, λ_s is the fast neutron slowing-down length, and L_t is the thermal neutron diffusion length.

Capture gamma rays are generated by thermal neutrons. Similar to the derivation of the inelastic gamma flux, the capture gamma flux can be expressed as

$$\phi_{\text{cap}\gamma}(R) = \frac{S_0 L_t^2 \sum_i^M N_i \int \sum_{\text{cap}\_i}}{4\pi R\left(\lambda_s^2 - L_t^2\right)} \left(e^{-R[1/\lambda_s - \alpha_1(1/\lambda_s - \mu\rho)]} - e^{-R[1/L_t - \alpha_2(1/\lambda_s - \mu\rho)]}\right), \tag{5}$$

where $\sum_{\text{cap}\_i}$ is the capture cross section of the ith nuclide.

Inelastic and capture gamma rays are represented separately in logarithmic form. From Eqs. (3) and (5), the gamma flux is affected by both neutron and gamma attenuation. The gamma attenuation is primarily influenced by the formation density, whereas the neutron attenuation is mainly influenced by the formation porosity. Therefore, by converting the fluxes to detector counts, we can approximate the detector counts as a function of the porosity, density, and source distance, as shown in Eq. (6):

$$\begin{cases} \ln N_{\mathrm{in}\gamma}(R,\varphi,\rho) = \ln \frac{S_0 \sum_i^M N_i \int \Sigma_{\mathrm{ine\_}i}}{4\pi R} + f(\varphi)(R\alpha - R) - R\alpha\mu\rho \\ \ln N_{\mathrm{cap}\gamma}(R,\varphi,\rho) = \ln \frac{S_0 L_{\mathrm{t}}^2 \sum_i^M N_i \int \Sigma_{\mathrm{cap\_}i}}{4\pi R\left(\lambda_{\mathrm{s}}^2 - L_{\mathrm{t}}^2\right)} + f(\varphi)\left(R\alpha_1 - R\right) + g(\varphi)\left(R\alpha_2 - R\right) + \mu\rho R\left(\alpha_2 - \alpha_1\right) \end{cases} \tag{6}$$

where $f(\varphi)$, $g(\varphi)$ are functions related to porosity (based on the transformation of diffusion or slowing-down length).

Based on Eq. (6), the intercepts of the curves when gamma varies with porosity (or density) are different because the elemental composition of the rocks varies with the lithology. The results shown in Fig. 4 are derived from the simulation results of the pulsed neutron tool presented in Sect. 3. With decreasing density (increasing porosity), the detector counts increase exponentially, matching the gamma attenuation trend. Figure 4b shows that the trend of capture gamma rays with porosity is essentially the same for different lithologies (only the intercept is different). This indicates that neutron decay is dominant for the capture gamma. To summarize, (1) neutron-induced gamma is affected by formation density, porosity, and lithology; (2) inelastic gamma is used for the measurement of formation density, whereas capture gamma reduces the sensitivity to formation density.

B. Time gate impact analysis

After analyzing the properties of the secondary gamma rays, it is necessary to investigate the composition of the capture and inelastic time spectra in the total time spectra. Owing to the periodic and repetitive nature of pulsed neutron sources, the following discussion is performed within a single-pulse period, as shown in Fig. 5.

From Fig. 5, the count collected according to the actual count can be expressed as

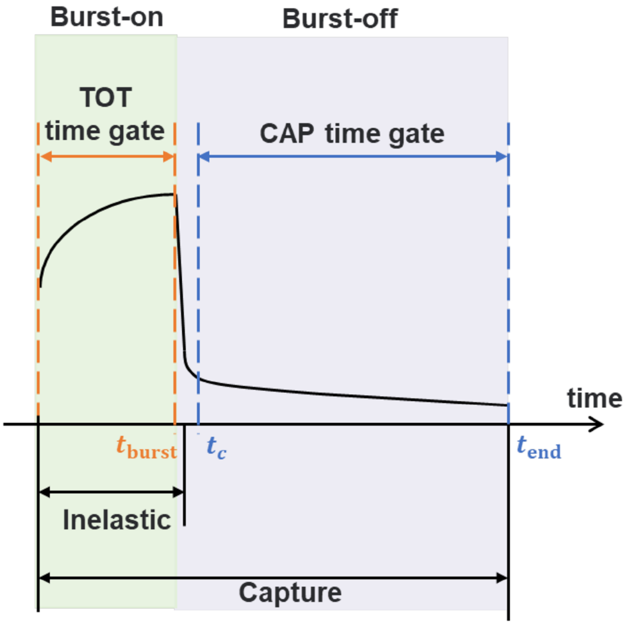

Fig. 5 (Color online) The duty cycle of the pulse sequence. TOT (total) time gate corresponds to the burst-on period and CAP (total) time gate corresponds to the time when only captures occur. t_{burst} corresponds to the duty cycle of the pulse neutron tube, t_{c} is related to the tool setting, and t_{end} is the end time of a pulse cycle, i.e., 100 µs

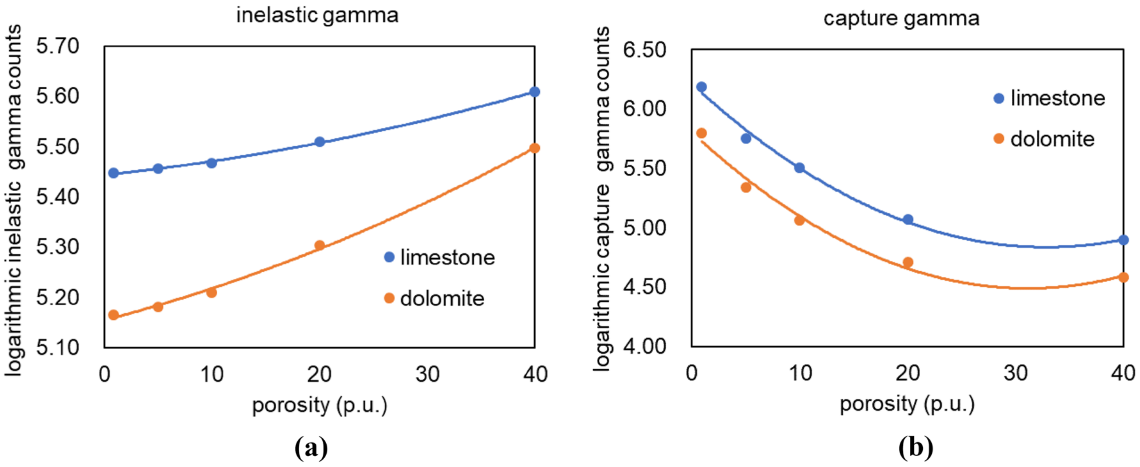

Fig. 4 (Color online) Inelastic and capture gamma changes with increasing porosity

$$\begin{cases} N_{\mathrm{TG\_TOT}\gamma} = \sum\limits_{t=0}^{t_{\mathrm{burst}}} TS(t) \\ N_{\mathrm{TG\_CAP}\gamma} = \sum\limits_{t=t_{\mathrm{burst}}+t_{\mathrm{c}}}^{t_{\mathrm{end}}} TS(t) \end{cases}, \tag{7}$$

where TS refers to the time spectra (μs), $N_{\mathrm{TG\_TOT}\gamma}$ is the gamma count in the burst-on period, and $N_{\mathrm{TG\_CAP}\gamma}$ is the (capture) gamma count in the burst-off period.

Because the inelastic gamma rays generated after the burst-on period decrease to zero, the composition of the time spectra can be expressed as

$$TS(t) = N_{\mathrm{in}\gamma}(t) + N_{\mathrm{cap}\gamma}(t) = \begin{cases} N_{\mathrm{in}\gamma}(t) + N_{\mathrm{cap}\gamma}(t) & (t \le t_{\mathrm{burst}}) \\ N_{\mathrm{cap}\gamma}(t) & (t > t_{\mathrm{burst}}) \end{cases}, \tag{8}$$

where $N_{\mathrm{in}\gamma}(t), N_{\mathrm{cap}\gamma}(t)$ are the detector counts of inelastic and capture gamma rays at time t, respectively.

Gamma time spectra during the burst-on and burst-off periods are derived separately to analyze the time gate impact on the capture and inelastic gamma. Suppose that fast neutrons are emitted uniformly during the burst-on period; that is, $k \times t$ fast neutrons are generated. Therefore, the relationship between gamma and time during the burst-on time gate can be expressed as

$$\begin{cases} \ln N_{\mathrm{in}\gamma}(t) = k\big(f(\varphi)(R\alpha - R) - R\alpha\mu\rho + c_1\big) \\ \ln N_{\mathrm{cap}\gamma}(t) = kt\big(f(\varphi)\big(R\alpha_1 - R\big) + g(\varphi)\big(R\alpha_2 - R\big) \\ \qquad\qquad +\mu\rho R\big(\alpha_2 - \alpha_1\big) + c_2\big) \end{cases} \quad t \le t_{\mathrm{burst}}, \tag{9}$$

where $c_1 = \ln\frac{S_0\sum_i^M N_i \int \Sigma_{\mathrm{ine\_}i}}{4\pi R}, c_2 = \ln\frac{S_0 L_{\mathrm{t}}^2 \sum_i^M N_i \int \Sigma_{\mathrm{cap\_}i}}{4\pi R(\lambda_{\mathrm{s}}^2 - L_{\mathrm{t}}^2)}$.

For the burst-off period, the time spectra can be approximated as the capture spectra based on Eq. (10):

$$\begin{cases} \ln N_{\mathrm{in}\gamma}(t) \approx 0 \\ \ln N_{\mathrm{cap}\gamma}(t) = \ln N_{\mathrm{cap}\gamma}\big(t_{\mathrm{burst}}\big) - R\big[\Sigma vt - \alpha_1(\Sigma vt - \mu\rho)\big] \end{cases} \quad t > t_{\mathrm{burst}}, \tag{10}$$

where Σ represents the macroscopic cross section and v is the neutron velocity.

Equations (8) and (9) show that the capture gamma collected in the TOT time gate increases with an increase in the burst time. Figure 6 shows an example of the simulation results obtained during the burst-on period under different duty cycles. The total counts during the burst-on period decreased with increasing porosity, which corresponded to increasing hydrogen content, indicating that neutron attenuation played a dominant role. During the burst-on period, the percentage of capture gamma rays increased with an increasing duty cycle, whereas with an increase in porosity, the proportion of capture gamma rays decreased. This demonstrates that the capture spectra parameters vary with changes in the duty cycle and environmental parameters.

In conclusion, the correction of the capture gamma contributes to obtaining counts where gamma attenuation dominates, thus improving the sensitivity of source-less density measurements to formations. Considering that the capture gamma is related to the duty cycle and environmental parameters during the burst-on period, an adaptive capture correction method is designed. This method is discussed in Sect. 2.2.

2.2 Burst-on period count optimization

A. Data pre-processing

The distribution of neutrons emitted by a pulsed neutron generator may be shaped differently than that

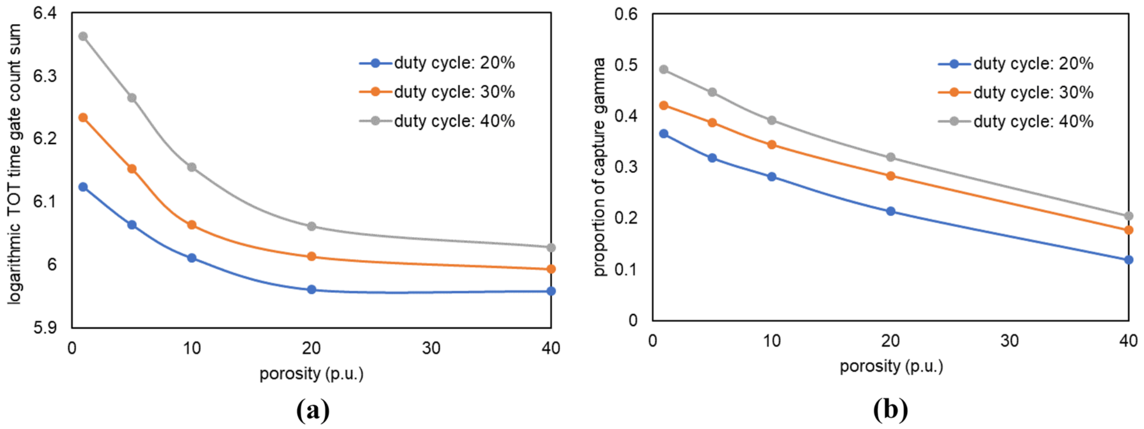

Fig. 6 (Color online) Effect of different duty cycles on the TOT time gate: **a**. Total counts under different duty cycles. The vertical coordinate refers to the logarithm of the counts. **b**. Proportion of capture gamma in the TOT time gate

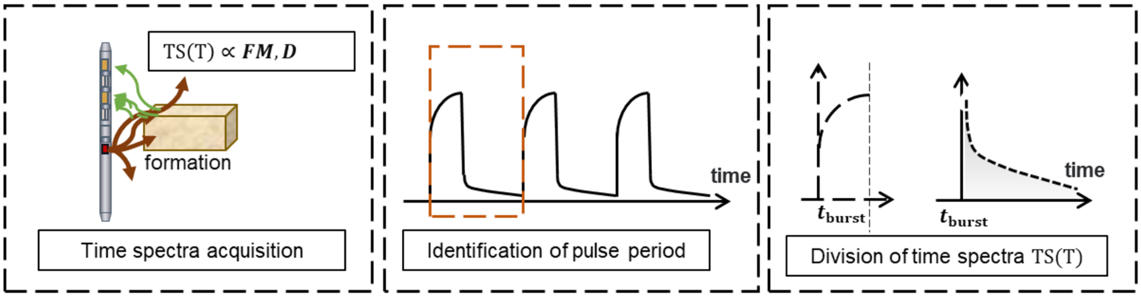

Fig. 7 (Color online) Data collection and preprocessing. ***FM***: Formation environment parameter, ***D***: duty cycle

controlled by electrical pulses, owing to hardware constraints. Therefore, it is necessary to first identify the pulse shape, that is, the end time (t_{burst}) of the burst-on period. Because no new fast neutrons are emitted during the burst-off period, the count of the time spectra collected after the burst-on period is significantly lower than that in the burst-on period; that is, the function $TS(t)$ is discontinuous and varies significantly at the end of the burst-on period. Therefore, the end time of the burst period can be determined by using an enumeration algorithm that compares the counts of adjacent samples within a pulse period, as shown in Eq. (11). Subsequently, the pulse shape can be matched and the time spectra can be divided, as shown in Fig. 7.

$$t_{\text{burst}} = \arg\max_{t} \frac{\partial TS(t)}{\partial t}, \quad t = 1, 2, \ldots, 100\,\mu\text{s}, \tag{11}$$

where TS denotes the time spectra and t denotes time (μs).

B. Capture gamma time spectra derivation

By identifying the width of the burst period t_{burst}, the time spectra of the capture gamma rays within a pulse period can be extracted from the total time spectra. The capture time spectra calculation process is shown in Fig. 8, and a detailed derivation is presented below.

As the capture spectra are continuous, it is assumed that the time spectra satisfy a Gaussian process. The time spectra within the TOT and CAP time gates are fitted using GPR.

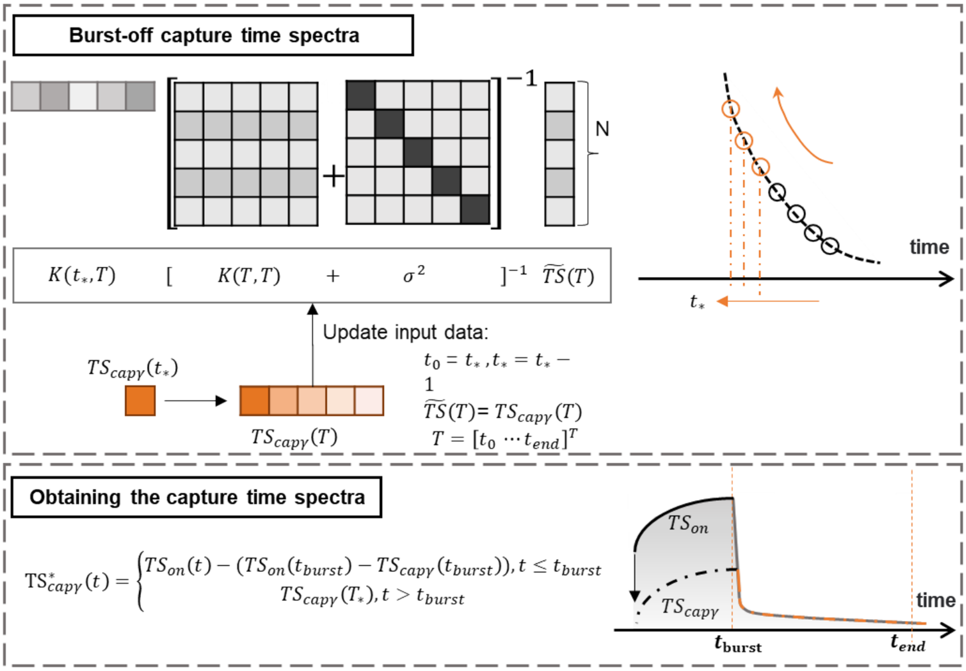

Fig. 8 (Color online) Obtaining the capture spectra based on GPR. Using the time spectra within the CAP time gate, the capture data within t_{burst}~t_{c} are calculated. One time point at a time is extrapolated to iteratively calculate the capture spectra under the burst-off period

$$\begin{cases} TS\left(T_{\text{on}}\right) \sim \text{GP}\left(\begin{bmatrix}0\\ \vdots \\ 0\end{bmatrix}, K_{\text{on}}\right), & T_{\text{on}} = \left[0, \ldots, t_{\text{burst}}\right] \\ TS\left(T_{\text{off}}\right) \sim \text{GP}\left(\begin{bmatrix}0\\ \vdots \\ 0\end{bmatrix}, K_{\text{off}}\right), & T_{\text{off}} = \left[t_{\text{c}}, \ldots, t_{\text{end}}\right] \end{cases}, \tag{12}$$

where T_{on} and T_{off} are the time-sampling points within the TOT and CAP time gates, respectively, and K_{on} and K_{off} are the corresponding covariance matrices.

The time spectra obtained using the CAP time gate are expressed as

$$TS\left(T_{\text{off}}\right) \sim \text{N}\left(\begin{bmatrix}0\\ \vdots \\ 0\end{bmatrix}, \begin{bmatrix} k\left(t_{\text{c}}, t_{\text{c}}\right) & \cdots & k\left(t_{\text{c}}, t_{\text{end}}\right) \\ \vdots & \ddots & \vdots \\ k\left(t_{\text{end}}, t_{\text{c}}\right) & \cdots & k\left(t_{\text{end}}, t_{\text{end}}\right) \end{bmatrix}\right), \tag{13}$$

$$k\left(t_i, t_j\right) = \sigma_{TS}^2 \exp\left(-\frac{\left(t_i - t_j\right)^2}{2l^2}\right), \tag{14}$$

where σ_{TS}^2, l are the hyperparameters in k. The larger σ_{TS}^2, the larger the variance.

Let $\theta = \{\sigma_{TS}, l\}$, then the corresponding hyperparameters are solved by maximizing the likelihood function, as shown in the following equation:

$$\theta = \arg\max_{\theta} \log p\left(TS\left(T_{\text{off}}\right) | t, \theta\right). \tag{15}$$

After establishing the GPR model based on the time spectra in the CAP time gate according to Eq. (15), the calculation of the capture gamma spectra at other time points can be expressed as Eq. (16) because the new time-point counts still obey the Gaussian distribution:

$$\begin{bmatrix} TS(T) \\ TS_{\text{cap}\gamma}\left(T_*\right) \end{bmatrix} \sim \text{N}\left(\begin{bmatrix} \mu \\ \mu_* \end{bmatrix}, \begin{bmatrix} K(T, T) & K\left(T, T_*\right) \\ K\left(T_*, T\right) & K\left(T_*, T_*\right) \end{bmatrix}\right), \tag{16}$$

where $T_* \in \left[t_{\text{burst}}, t_{\text{c}}\right)$, $T \in T_{\text{off}}$.

The calculated distribution of the capture gamma rays in the burst-off period is given by

$$TS_{\text{cap}\gamma}\left(T_*\right) \sim \mathcal{N}\left(\mu_*, \Sigma_*\right), \tag{17}$$

where

$$\begin{aligned} \mu_* &= K\left(T_*, T\right)\left(K(T, T) + \sigma^2\right)^{-1} TS(T), \\ \Sigma_* &= K\left(T_*, T_*\right) + \sigma^2 - K\left(T_*, T\right)\left(K(T, T) + \sigma^2\right)^{-1} K\left(T, T_*\right). \end{aligned} \tag{18}$$

To further illustrate these steps, the simulation results with a duty cycle of 30% is used as an example. Figure 9 shows the calculation of the capture gamma rays during the burst-off period, using the total time spectra as the input. The true capture spectra (obtained by Geant4 physical process identification) are shown in blue, and the calculated results are shown in red. Capture spectra can be obtained after matching the burst-on periods in the same manner. After matching, the capture spectra within a single-pulse period are obtained using Eq. (19):

$$\text{TS}^*_{\text{cap}\gamma}(t) = \begin{cases} TS_{\text{on}}(t) - \left(TS_{\text{on}}\left(t_{\text{burst}}\right) - TS_{\text{cap}\gamma}\left(t_{\text{burst}}\right)\right), & t \le t_{\text{burst}} \\ TS_{\text{cap}\gamma}(t), & t > t_{\text{burst}} \end{cases}. \tag{19}$$

The capture counts at time point t_{burst} are jointly determined with the calculated results under the burst-on and burst-off periods, thus adjusting Eq. (17) again. The distribution of capture gamma rays over time is obtained using Eq. (19), as shown in Fig. 10.

C. Density measurement

The inelastic gamma time spectra are obtained by subtracting the capture spectra from the total time spectra, that is, the net inelastic gamma count is obtained, as shown in Eq. (20). Because the capture spectra are derived from the total time spectra, the method can be adapted to different porosities and densities of the formation, as well as different duty cycles of the neutron source:

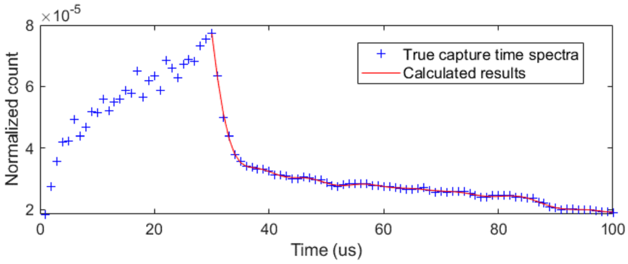

Fig. 9 Comparison between calculated and true values of capture time spectra during the burst-off period

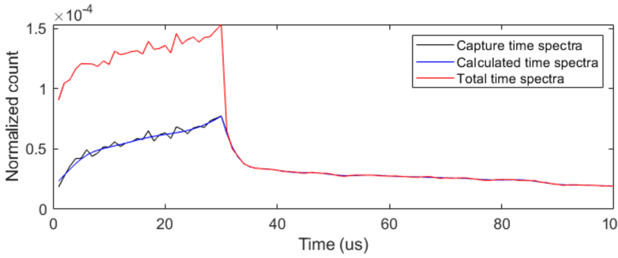

Fig. 10 (Color online) Comparison of the calculated capture spectra to true capture and total time spectra per pulse cycle

$$N_{\text{nin}\gamma} = \sum_{t=0}^{t_{\text{burst}}} TS_{\text{ine}\gamma}(t) = \sum_{t=0}^{t_{\text{burst}}} \left(TS(t) - TS^{*}_{\text{cap}\gamma}(t)\right), \tag{20}$$

where $N_{\text{nin}\gamma}$ is the net inelastic gamma obtained from the calculated inelastic time spectra $TS_{\text{ine}\gamma}(t)$.

The algorithm below describes the calculation of the net inelastic gamma. This algorithm can be applied to both near and far source detectors to calculate the count ratio for the acquisition of the formation density.

Algorithm: Acquisition of adaptive net inelastic gamma

Input: total time spectra TS

Output: net inelastic gamma count ratio $N_{nin\gamma}$

```
Initialize $t$, $t_{burst}$, $LOSS$
for $t < 100$ do
    Compute the loss function: $LOSS = \frac{\partial TS(t)}{\partial t}$
    if LOSS is maximum value, then
        $t_{burst} = t$
    end
end
for $t = t_c$ ; $t > t_{burst}$ do
    Calculate burst-off capture gamma time spectra with GPR: $TS_{\text{cap}\gamma}(T_*)$
    $t = t - 1$
end
Match the burst-on time spectra $TS_{on}(T)$
Calculate burst-on capture gamma time spectra: $TS_{on}(T) - (TS_{on}(t_{burst}) - TS_{\text{cap}\gamma}(t_{burst}))$
Calculate net inelastic gamma counts: $N_{nin\gamma} = \sum_{t=0}^{t_{burst}}(TS(t) - TS^{*}_{\text{cap}\gamma}(t))$
```

For a single detector, formation density ρ is expressed as

$$\rho = \frac{1}{R\alpha\mu}\left[\ln\frac{S_0 \sum_i^M N_i \int \sum_{\text{in\_}i}}{4\pi R} - R(1-\alpha)1/\lambda_{\text{s}} - \ln\phi_{\text{in}\gamma}(R,\varphi,\rho)\right]. \tag{21}$$

For an established tool structure for source-less density measurements, that is, two gamma detectors and two thermal neutron detectors, to correct the influence of the hydrogen index on the density measurement, formulae (21) can be further written as

$$\rho = A \cdot \ln\frac{N_{\text{in}\gamma_1}}{N_{\text{in}\gamma_2}} + B \cdot \ln\frac{N_{\text{n}_1}}{N_{\text{n}_2}} + C, \tag{22}$$

where $N_{\text{in}\gamma_1}$ and $N_{\text{in}\gamma_2}$ are the counts of near and far gamma detectors after capture correction, respectively; N_{n_1} and N_{n_2} are counts of near and far neutron detectors, respectively; and A, B, and C are constant coefficients.

Table 1 Parameters of the simulation models

Lithology	Porosity (p.u.)	Pore fluid	Duty cycle	Borehole diameter (mm)
Dolomite	0.9–40	Water, oil, gas	20%, 30%, 40%	216
Limestone	0.9–40	Water, oil, gas	20%, 30%, 40%	216
Sandstone	0.9–40	Water, oil, gas	20%, 30%, 40%	216
Anhydrite	0.9–40	Water, oil, gas	20%, 30%, 40%	216
Illite	0.9–40	Water, oil, gas	20%, 30%, 40%	216
Kaolinite	0.9–40	Water, oil, gas	20%, 30%, 40%	216
Montmorillonite	0.9–40	Water, oil, gas	20%, 30%, 40%	216
Chlorite	0.9–40	Water, oil, gas	20%, 30%, 40%	216

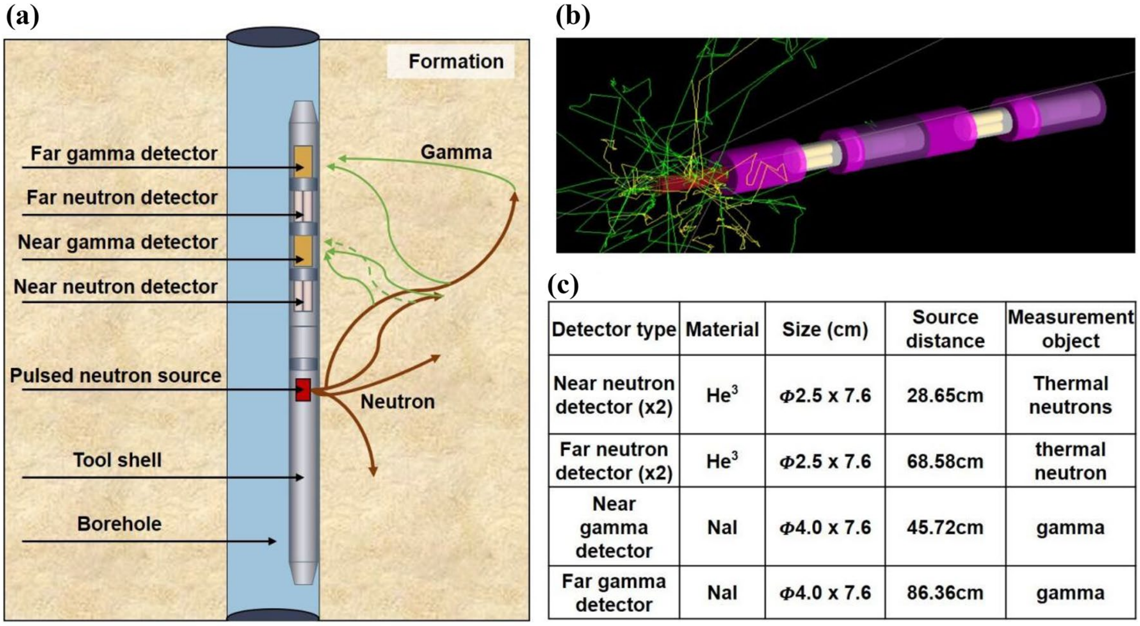

Detector type	Material	Size (cm)	Source distance	Measurement object
Near neutron detector (x2)	He^3	Φ2.5 x 7.6	28.65cm	Thermal neutrons
Far neutron detector (x2)	He^3	Φ2.5 x 7.6	68.58cm	thermal neutron
Near gamma detector	NaI	Φ4.0 x 7.6	45.72cm	gamma
Far gamma detector	NaI	Φ4.0 x 7.6	86.36cm	gamma

Fig. 11 (Color online) Overview of the source-less density tool model. a. Schematic diagram of the tool structure. b. Geant4 simulation. c. Detector parameters

3 Verification using Monte Carlo modelling

Based on theoretical derivations, the pulsed neutron density logging is influenced by formation parameters and the duty cycle of the pulsed neutron tube. To test the applicability and adaptiveness of the method, a dataset of 288 models with different parameters is simulated, as presented in Table 1. Because most pulsed-neutron density measurements use a 20% duty cycle while other pulsed neutron applications use a 30% duty cycle, 20%, 30%, and 40% are chosen to verify the adaptability of the method to the duty cycle (a significantly high duty cycle is not conducive to the collection of inelastic gamma rays). The source-less density tool has four sets of detectors, as shown in Fig. 11. Both gamma detectors are sodium iodide detectors, and the far and near neutron detectors consisted of two He^3 tubes.

The simulation collects the time spectra of the gamma as an input, whereas pure inelastic gamma is collected as a reference through physical process identification. The method is validated in two progressive parts: detector count ratio and density calculations.

3.1 Calculation of the inelastic count ratio

Because the count ratio can minimize the effect of the in-well environment on the tool response and improve its sensitivity to formation, it is used in the calculation of the formation density, as shown in Eq. (22). Thus, the method is validated using detector count ratio R_γ as given Eq. (23):

$$R_\gamma = \frac{N_{\text{in}\gamma_1}}{N_{\text{in}\gamma_2}}. \tag{23}$$

where $N_{\text{in}\gamma_1}$ and $N_{\text{in}\gamma_2}$ are near and far detector counts, respectively.

The statistical error of the count ratio obtained from the simulation can be calculated using Eq. (24):

$$SE = \sqrt{\frac{1}{N_{\text{in}\gamma_1}} + \frac{1}{N_{\text{in}\gamma_2}}} \times 100\% \tag{24}$$

where SE refers to a statistical error.

For the count ratios, the relative error is used to evaluate the calculated results expressed in Eq. (25). When the relative error between the calculated and simulation results is less than the statistical error of the simulation data, the calculated results satisfied the accuracy.

$$RE = \frac{|PRE - MC|}{MC} \times 100\%, \tag{25}$$

where PRE is the calculated count ratio, MC is the simulated count ratio, and RE is the relative error.

The relative error between the calculated count ratio and the true value is less than the statistical error in 281 out of

Table 2 Comparison results pertaining to different duty cycles under limestone

Duty cycle (%)	Porosity (p.u.)	True count ratio	Calculated count ratio	Statistical error (%)	Relative error (%)
20	0.9	66.71	65.63	4.01	1.62
	10	65.83	65.44	3.87	0.59
	20	58.53	57.35	3.91	2.02
	40	51.33	52.66	3.56	2.59
30	0.9	65.4	67.62	3.77	3.39
	10	64.55	65.11	3.66	0.87
	20	58.33	57.34	3.50	1.70
	40	53.28	53.89	3.66	1.14
40	0.9	65.92	67.22	3.79	1.97
	10	65.55	66.17	3.60	0.95
	20	57.33	56.21	3.57	1.95
	40	52.28	52.19	3.78	0.17

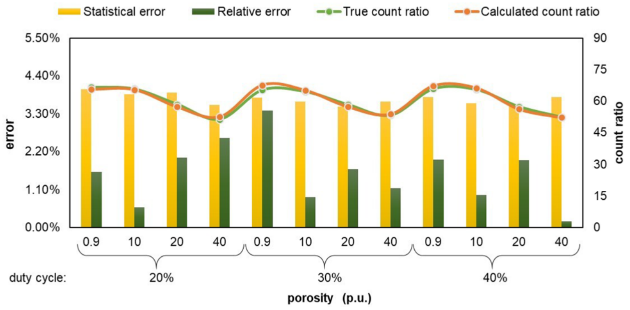

Fig. 12 (Color online) Comparison between the detector count ratio and error at different duty cycles (limestone)

the 288 data points (97.6%), which indicates that the method can effectively correct the effect of capture. Part of the data that did not satisfy the error is related to the case where the duty cycle is 40% (the larger the duty cycle, the greater the impact of capture). To further test the applicability of the method, the results are discussed for three cases: the impact of (1) the duty cycle, (2) environmental parameters, and (3) multiparameter variation.

3.1.1 Case1: Duty cycle impact analysis

In this case, the formation lithology is limestone and the pores are filled with freshwater. The results obtained for the different duty cycles are presented in Table 2 and Fig. 12.

As shown in Fig. 12, the net inelastic gamma count ratio decreases with increasing porosity. The trend of the net inelastic gamma count ratio with porosity is similar at different duty cycles, which indicates that the duty cycle does not affect the source-less density measurements using the

Table 3 Comparison results for different lithology

Lithology	Porosity (p.u.)	True count ratio	Calculated count ratio	Statistical error (%)	Relative error (%)
Dolomite	0.9	85.4	84.62	3.01	0.91
	20	80.53	78.35	2.86	2.71
Sandstone	0.9	67.34	67.64	3.07	0.45
	20	60.45	62.09	2.96	2.71
Anhydrite	0.9	77.65	78.41	4.68	0.98
	20	65.89	65.63	4.39	0.39
Illite	0.9	88.65	91.39	4.49	3.09
	20	73.47	75.69	4.69	3.02
Kaolinite	0.9	77.44	74.67	4.84	3.58
	20	64.65	66.88	4.88	3.45
Montmorillonite	0.9	70.26	68.57	4.41	2.41
	20	65.27	63.25	4.53	3.09
Chlorite	0.9	75.65	76.1	4.17	0.59
	20	66.76	64.17	4.29	3.88

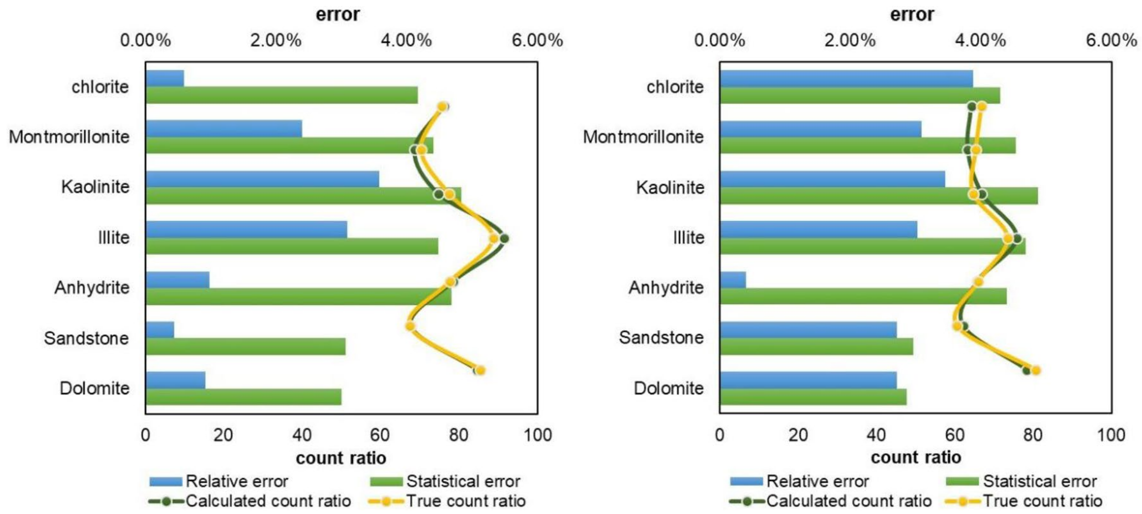

Fig. 13 (Color online) Comparison of the detector count ratio and error for different lithology. The porosity is 0.9 p.u. in the left and 20 p.u. in the right figure

Table 4 Comparison results for different pore fluids in dolomite

Pore fluid	Porosity (p.u.)	True count ratio	Calculated count ratio	Statistical error (%)	Relative error (%)
Oil	0.9	86.63	83.57	3.83	3.53
Oil	5	84.41	85.58	3.11	1.39
Oil	20	78.94	81.13	3.70	2.77
Oil	30	68.91	70.28	3.43	1.99
Oil	40	63.38	65.27	3.33	2.98
Gas	0.9	77.68	75.78	3.65	2.45
Gas	5	70.67	68.87	3.47	2.55
Gas	20	55.67	57.14	3.01	2.64
Gas	30	47.11	48.26	2.71	2.44
Gas	40	36.7	37.23	2.39	1.44
Water	0.9	88.4	86.62	3.37	2.01
Water	5	85.13	84.63	3.41	0.59
Water	20	81.42	80.35	3.67	1.31
Water	30	70.41	71.76	3.79	1.92
Water	40	62.13	61.1	3.56	1.66

inelastic gamma count ratio. Comparing the statistical error of the true ratio and the relative error, the relative errors of all the test data in limestone are less than the statistical errors, which shows that the proposed method can effectively deduce the capture under different duty cycles.

3.1.2 Case2: Environmental parameters impact

A. Lithology variation

Because lithology has a large influence on gamma attenuation, particularly the capture gamma, the results obtained under eight different lithologies are compared in this case

Fig. 14 (Color online) Comparison between the detector count ratio and error for different pore fluids

(except for dolomite and sandstone, which all belong to the mineral category). In this case, the duty cycle is 20%, and the pore fluid is water.

Secondary gamma production is correlated with the corresponding element (as shown in Eq. 2), the lithology has a strong influence on the detector count ratio. Table 3 and Fig. 13 present the results of the inelastic gamma compared with the capture-corrected inelastic gamma. In terms of relative errors, the errors are relatively higher for various types of minerals. For example, chlorite-containing iron also increases capture counts. These results illustrate that this method can also be applied to acquire net inelastic gamma under different lithologies.

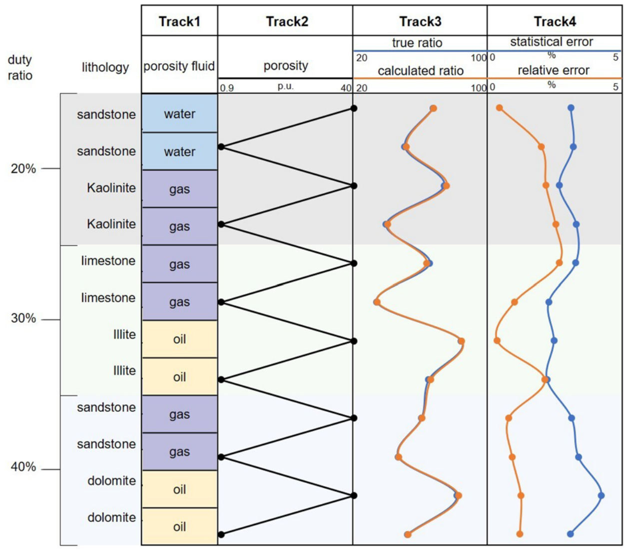

Fig. 15 (Color online) Comparison of the detector count ratio at different duty cycles and environment parameters

B. Pore fluid variation

The formation fluids typically include oil, gas, and water. Among them, gas contains a much lower hydrogen index than oil and water, which affects the attenuation of neutrons at different porosities, thus affecting the distribution of secondary gamma rays. This case is used to verify the adaptiveness of the capture correction method under different pore fluids by varying the pore fluid type using dolomite and a 30% duty cycle (to avoid duplication of data). A comparison of the results is presented in Table 4 and Fig. 14. Because the gas density is the lowest, the gamma decay is the weakest at the same porosity. The hydrogen index of the gas is also the lowest, and the neutron attenuation is still the weakest. The final count ratios of the three pore fluids are shown in Fig. 14; the order of the detector count ratios under the same porosity is water > oil > gas. In addition, the count ratio under gas varied the most with porosity. Overall, the relative errors are less than the statistical errors of all the results, which indicates that the capture correction method can effectively correct the capture at different pore fluids.

3.1.3 Case3: Duty cycle, lithology, pore fluid variation

In this case, the duty cycle, lithology, and pore fluid are changed to further verify the accuracy of the net inelastic gamma count ratio obtained using the capture gamma correction method. As shown in Fig. 15 and Table 5, the 12 sets of samples consisted of three duty cycles, five lithologies, and three pore fluids.

The results shown in Fig. 15, Track4, indicate that the proposed method can effectively adapt to different duty cycles and environmental parameters. Relative errors (orange line) are less than absolute errors (blue line), demonstrating the

Table 5 Comparison results for different duty cycles and environment parameters

Duty cycle (%)	Lithology	Pore fluid	Porosity (p.u.)	True count ratio	Calculated count ratio	Statistical error (%)	Relative error (%)
20	Sandstone	Water	0.9	67.34	67.64	3.07	0.45
20	Sandstone	Water	40	50.52	51.52	3.17	1.98
20	Kaolinite	Gas	0.9	73.73	75.32	2.65	2.16
20	Kaolinite	Gas	40	39.47	40.46	3.28	2.51
30	Limestone	Gas	0.9	65.23	63.5	3.26	2.65
30	Limestone	Gas	40	33.99	34.33	2.26	1.00
30	Illite	Oil	0.9	83.86	84.15	2.45	0.35
30	Illite	Oil	40	64.71	66.08	2.19	2.12
40	Sandstone	Gas	0.9	60.43	60.9	3.11	0.78
40	Sandstone	Gas	40	46.73	47.15	3.35	0.90
40	Dolomite	Oil	0.9	81.3	82.3	4.20	1.23
40	Dolomite	Oil	40	52.07	52.69	3.05	1.19

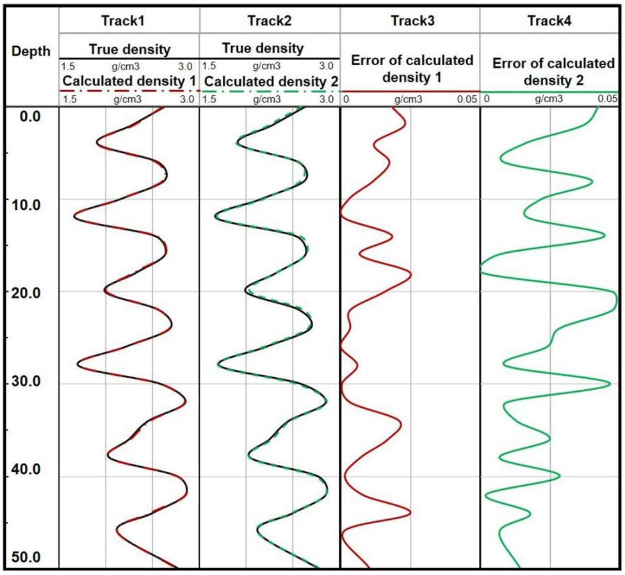

Fig. 16 (Color online) Formation density calculation results at 20% duty cycle. Track1: Comparison of the true density with the formation density calculated using inelastic gamma count ratios through capture correction method. Track2: Comparison of the true density with the formation density calculated using burst-on count ratios. Track3: Absolute error = |true density − calculated density 1|. Track4: Absolute error = |true density − calculated density 2|

adaptability of the method. The following conclusions can be made:

- The duty cycle of the system directly affects the proportion of capture during the burst period. Moreover, increasing the duty cycle results in a higher proportion of capture; however, this can reduce the accuracy of subsequent formation density measurements.
- The lithology has a significant impact on the distribution of the secondary gamma field.
- Differences in pore fluids affect the neutron field distribution, causing an increased slowing of neutrons by the medium and reduced capture gamma rays reaching the detector.

3.2 Formation density calculation

Most current pulsed neutron density algorithms use inelastic gamma rays [24, 25]. However, the net inelastic gamma ray may not always be acquired as an input for practical applications, which increases the error of the density measurement algorithm. To demonstrate the practicality of the capture gamma correction method, the formation densities are calculated separately using the corrected count ratios versus the original count ratios (Eq. 22). Because the density accuracy is an important index for evaluating density measurement-related methods, the calculated formation densities are compared with the true densities to illustrate the differences before and after the application of the method. Most pulsed neutron density logging uses a duty cycle of 20%; therefore, this is selected as the modelling parameter. Figure 16 shows the results of the density calculations for this case. The model shown in the figure contains seven rocks: limestone, sandstone, dolomite, anhydrite, illite, kaolinite, and montmorillonite. The pore fluids are fresh water, methane, and oil. The formation bulk density ranged from 1.67 to 2.87 g/cm^3.

In Fig. 16, the errors of the formation density calculated after the capture correction are all less than 0.025 g/cm^3, whereas only 64% of the formation density results calculated using uncorrected gamma have an error of less than 0.025 g/cm^3. In addition to absolute errors, the RMSE (Eq. 26) is used as an indicator to evaluate the density accuracywhere *num* is the number of samples,

$$RMSE = \sqrt{\frac{1}{num}\sum_{i=1}^{n}\left(y_i - \hat{y}_i\right)^2}, \tag{26}$$

y_i denotes calculated density, and $\hat{y}_i$ denotes true density.

The RMSE of the formation density calculated after the capture correction is 0.013 g/cm^3, while the RMSE of the formation density calculated using burst-on count ratios is 0.025 g/cm^3. The absolute error of the results obtained using the method proposed in this study is less than 0.025 g/cm^3, and its RMSE is smaller than the RMSE without the capture correction, indicating that the method can effectively improve the accuracy of source-less density logging.

4 Conclusion

Conventional density measurement methods that use radioactive isotopes carry significant risks, including environmental contamination. Consequently, there is a growing interest in using manually controlled pulsed-neutron sources as an alternative method for source-less density measurements. However, the accuracy of source-less density measurements can be compromised by the presence of capture gamma rays during the neutron burst-on period. To overcome this challenge, this study introduced an adaptive capture gamma correction method for complex and diverse formation environments with varying pulse duty cycles. The results are as follows:

(1) The differential of the time spectra was calculated to identify and match the different neutron pulsed duty cycles. The capture time spectrum was calculated by introducing GPR, and the net inelastic gamma was obtained.
(2) For validation, a theoretical density tool was employed at different duty cycles in simulated environments with different porosities, pore fluids, and lithologies (288 model sets). Compared to the true inelastic gamma collected using the physical process, a consistent net inelastic gamma was obtained in 97.6% of the models under different environments and pulse duty cycles using the proposed method, which demonstrates the adaptability of the method.
(3) The errors of the formation density calculated after the capture correction were all less than 0.025 g/cm^3, whereas only 64% of the formation density results calculated using uncorrected gamma had an error of less than 0.025 g/cm^3.

These results show that the proposed method can effectively improve the accuracy of source-less density logging when the duty cycle and formation environment change. In future work, the feasibility of the proposed method will be explored further using a designed source-less density tool and field tests.

Author contributions All authors contributed to the study conception and design. Material preparation, data collection and analysis were performed by Yi Ge and Yu-Lian Li. The first draft of the manuscript was written by Yi Ge and Yu-Lian Li, and Qiong Zhang commented on previous versions of the manuscript. All authors read and approved the final manuscript.

Data availability The data that support the findings of this study are openly available in Science Data Bank at https://doi.org/10.57760/sciencedb.j00186.00131 and https://cstr.cn/31253.11.sciencedb.j00186.00131.

Declarations

Conflict of interest The authors declare that they have no competing interests.

References

1. D.V. Ellis, J.M. Singer, *Well logging for earth scientists*, vol. 692 (Springer, Dordrecht, 2007)
2. Q. Zhang, J. Liang, X. Wang et al., Dracarys: high-fidelity nuclear well logging benchmark problems with experimental results. Ann. Nucl. Energy **173**, 109116 (2022). https://doi.org/10.1016/j.anucene.2022.109116
3. Q. Zhang, Y. Li, Y. Jin et al., A new gamma density measurement method for cased-hole formation evaluation. Appl. Radiat. Isotopes **184**, 110178 (2022). https://doi.org/10.1016/j.apradiso.2022.110178
4. A. Badruzzaman, An assessment of fundamentals of nuclear-based alternatives to conventional chemical source bulk density measurement. Petrophysics **55**, 415–434 (2014)
5. A. Gilchrist, F. Inanc, L. Roberts, Nuclear source replacement-promises and pitfalls, in *SPWLA 52nd Annual Logging Symposium*, (Colorado, 2011).
6. Y. Ge, J. Liang, Q. Zhang et al., A comparison study of GEANT4 and MCNP6 on neutron-induced gamma simulation. Appl. Radiat. Isotopes **190**, 110514 (2022). https://doi.org/10.1016/j.apradiso.2022.110514
7. H.W. Yu, Y.X. Zhang, X.H. Chen et al., Numerical simulation and method study of X-ray litho-density logging. Nucl. Sci. Tech. **31**(12), 124 (2020). https://doi.org/10.1007/s41365-020-00826-2
8. L. Zhang, H.W. Yu, Y. Li et al., Improved formation density measurement using controllable DD neutron source and its lithological correction for porosity prediction. Nucl. Sci. Tech. **33**(1), 3 (2022). https://doi.org/10.1007/s41365-022-00988-1
9. M. Simon, A. Tkabladze, S. Beekman et al., A novel X-ray tool for true sourceless density logging. Petrophysics **59**(05), 565–587 (2018). https://doi.org/10.30632/PJV59N5-2018a1
10. G. Schmid, R. Pemper, D. Dolliver et al., A diffusion-corrected sigma algorithm for a four-detector pulsed-neutron logging tool, in *SPE Annual Technical Conference and Exhibition*, (Texas, 2018). Doi: https://doi.org/10.2118/191738-MS
11. D. Rose, T. Zhou, S. Beekman et al., An innovative slim pulsed neutron logging tool, in *SPWLA 56th Annual Logging Symposium*, (California, 2015)
12. X. Fu, W. Wu, H. Wang et al., A new neutron-gamma porosity measurement method for pulsed neutron logging tools. Geophysics **88**(4), 1–55 (2023). https://doi.org/10.1190/geo2022-0471.1
13. G. Xing, Q. Zhang, N. Li et al., A LWD gas-reservoir recognition method based on the inelastic gamma information of the drill collar. Geoenergy Sci. Eng. **225**, 211684 (2023). https://doi.org/10.1016/j.geoen.2023.211684
14. Q. Liang, F. Zhang, J. Fan, et al., A novel gamma-thermal neutron evaluating gas saturation method using pulsed neutron logging tool with dual-CLYC, in *SPWLA 63rd Annual Logging Symposium. OnePetro*, (Norway, 2022). Doi: https://doi.org/10.30632/SPWLA-2022-0078
15. W. Tang, J.G. Liang, Y. Ge et al., A method for neutron-induced gamma spectra decomposition analysis based on Geant4 simulation. Nucl. Sci. Tech. **33**(12), 154 (2022). https://doi.org/10.1007/s41365-022-01144-5
16. F. Inanc, Pulsed neutron generator-driven sourceless density measurements-expectations, physics and issues, in *SPWLA 55th Annual Logging Symposium*, (United Arab Emirates, 2014)
17. Q. Zhang, F. Zhang, C. Yuan et al., A comparative study on the neutron-gamma density and gamma-gamma density logging. J. Petrol. Sci. Eng. **176**, 792–799 (2019). https://doi.org/10.1016/j.petrol.2019.02.007
18. N. Reichel, M. Evans, F. Allioli et al., Neutron-gamma density (NGD): principles, field test results and log quality control of a radioisotope-free bulk density measurement, in *SPWLA 53rd Annual Logging Symposium*, (Colombia, 2012)
19. N. Reichel, M. Evans, F. Allioli et al., Sourceless neutron-gamma density (SNGD): principles, field-test results and log quality control of a radioisotope-free bulk-density measurement. Petrophysics **54**(02), 91–103 (2013)
20. M. Evans, F. Allioli, V. Cretoiu et al., Sourceless neutron-gamma density SNGD: a radioisotope-free bulk density measurement: physics principles, environmental effects, and applications, in *SPE Annual Technical Conference and Exhibition*, (Texas, 2012). Doi: https://doi.org/10.2118/159334-MS

21. Q. Zhang, F. Zhang, J. Liu et al., A method of determining formation density based on fast-neutron gamma coupled field theory. Petrophysics **58**, 411–425 (2017)
22. H. Wang, W. Wu, T. Tang et al., A new method for calculating bulk density in pulsed neutron-gamma density logging. Geophysics **85**(6), D219–D232 (2020). https://doi.org/10.1190/geo2018-0821.1
23. Q. Zhang, R. Deng, S. Zhang et al., An alternative method for sourceless density measurement with boron sleeve gamma detectors. Appl. Radiat. Isotopes **174**, 109785 (2021). https://doi.org/10.1016/j.apradiso.2021.109785
24. D. Dong, W. Wu, W. Yue et al., Improving the pulsed neutron-gamma density method with machine learning regression algorithms. J. Petroleum Sci. Eng. **218**, 110962 (2022). https://doi.org/10.1016/j.petrol.2022.110962
25. Q. Zhang, F. Zhang, C. Yuan et al., Application analysis on the different neutron gamma density (NGD) logging methods. Appl. Radiat. Isotopes. **172**, 109672 (2021). https://doi.org/10.1016/j.apradiso.2021.109672
26. C. Stoller, B. Adolph, M. Berheide et al., Use of $LaBr_3$ for downhole spectroscopic applications. in 2011 IEEE Nuclear Science Symposium Conference Record, Valencia, Spain, 2011, pp. 191–195. https://doi.org/10.1109/NSSMIC.2011.6154477
27. C. Yuan, C. Li, C. Zhou et al., Can the evaluation accuracy of elemental concentration be further enhanced in geochemical logging?—A break attempt to obtain purer inelastic gamma spectrum, in *SPWLA 60th Annual Logging Symposium*, (Texas, 2019). https://doi.org/10.30632/T60ALS-2019_DDDD
28. R. C. Odom, U.S. Patent No. 5,374,823, 20 Dec 1994
29. G. Schmid, R. Pemper, D. Dolliver et al., A new cased-hole porosity measurement for a four-detector pulsed-neutron logging tool, in *SPE Annual Technical Conference and Exhibition*, (Alberta, 2019). https://doi.org/10.2118/195950-MS
30. F. Li, X. Han, F. Mendez, Sigma measurement and applications with a pulsed-neutron mineralogy instrument, in *SPWLA 52nd Annual Logging Symposium*, (Colorado, 2011)
31. E. Schulz, M. Speekenbrink, A. Krause, A tutorial on Gaussian process regression: Modelling, exploring, and exploiting functions. J. Math. Psychol. **85**, 1–16 (2018)